Supplemental Information

Bridging Redox Asymmetry in Hot and Cold Cells for Boosted Power Density in Thermally Regenerative Flow Batteries

Huan Gao [a], Yuhao Cai [a], Wei Xiao [a], Mingming Yin [a], Minjie Liu [c], Tianshou Zhao [b,*], Haoran Jiang [a,d,*]

[a] State Key Laboratory of Engines, Tianjin University, Tianjin 300072, China

[b] Shenzhen Key Laboratory of Advanced Energy Storage, Department of Mechanical and Energy Engineering, Southern University of Science and Technology, Shenzhen 518055, China

[c] School of Mechanical Engineering, Tiangong University, Tianjin 300387, China

[d] National Industry-Education Platform of Energy Storage, Tianjin University, Tianjin 300072, China

* Corresponding authors: zhaots@sustech.edu.cn; jianghaoran@tju.edu.cn

Supplemental Figures

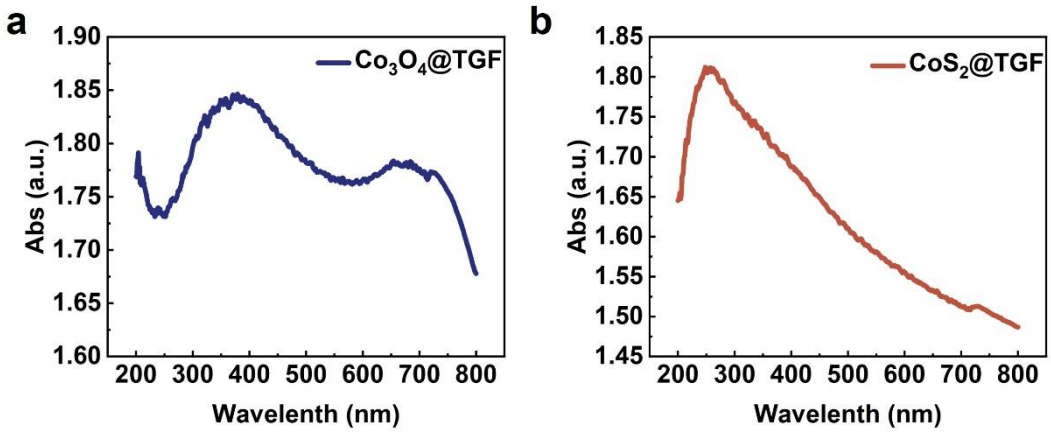

Fig. S1 Ultraviolet/Visible/Near-Infrared Diffuse Reflection Spectroscopy (UV-Vis DRS) of (a) Co_3O_4@TGF and (b) CoS_2@TGF.

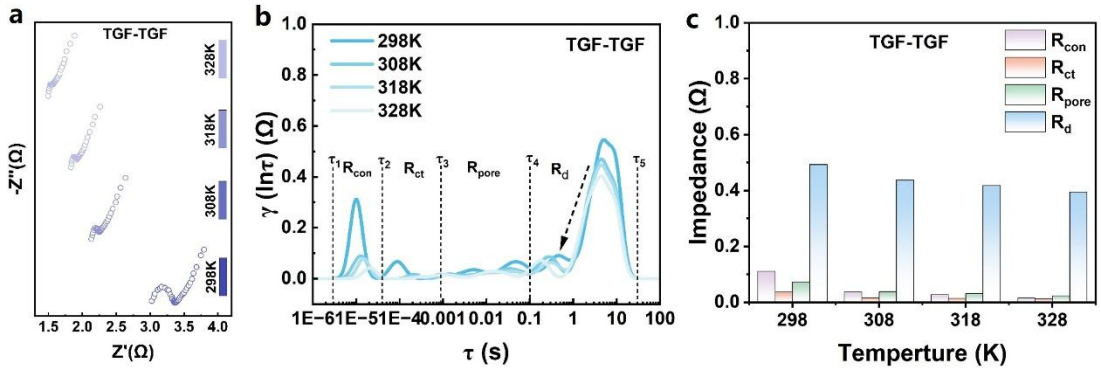

Fig. S2 (a) In situ EIS and (b) DRT plots of TGF-TGF in TRFB test under variable temperatures. (c) The corresponding impedance distribution.

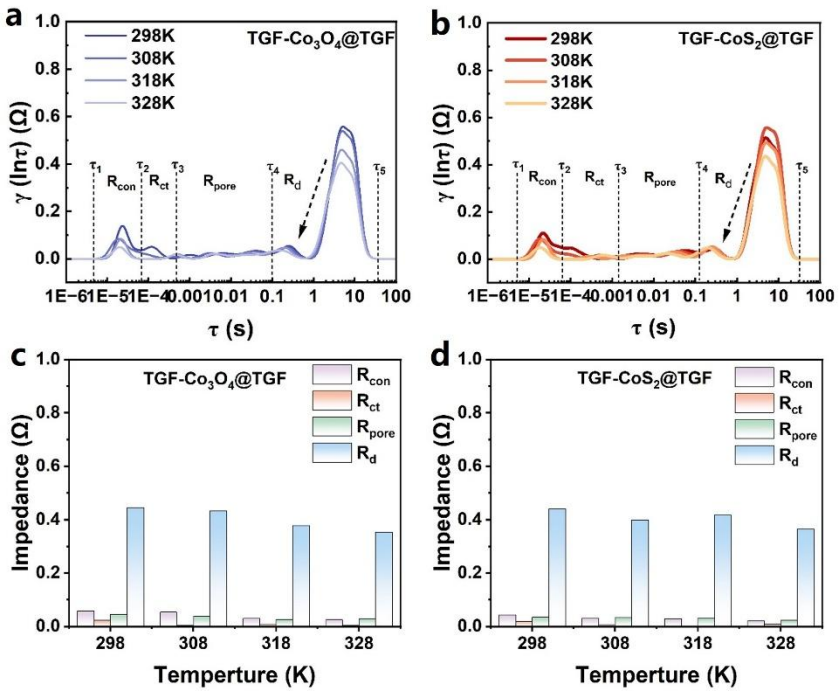

Fig. S3 The DRT results for the TRFB with electrode configurations of (a) TGF-Co_3O_4@TGF and (b) TGF-CoS_2@TGF under various temperatures. (c) and (d) The corresponding impedance distribution.

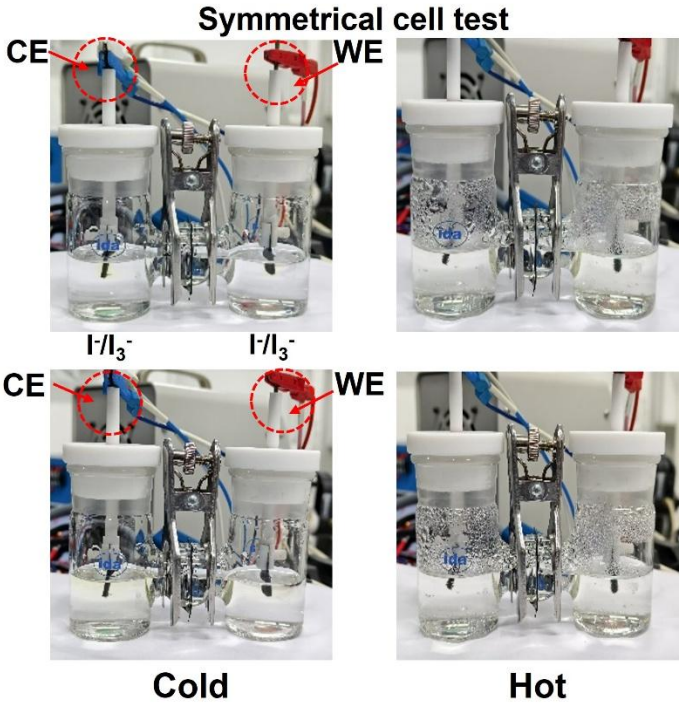

Fig. S4 Symmetric cell tests through a two-electrode system based on 0.01 M KI + 1 M KCl solution.

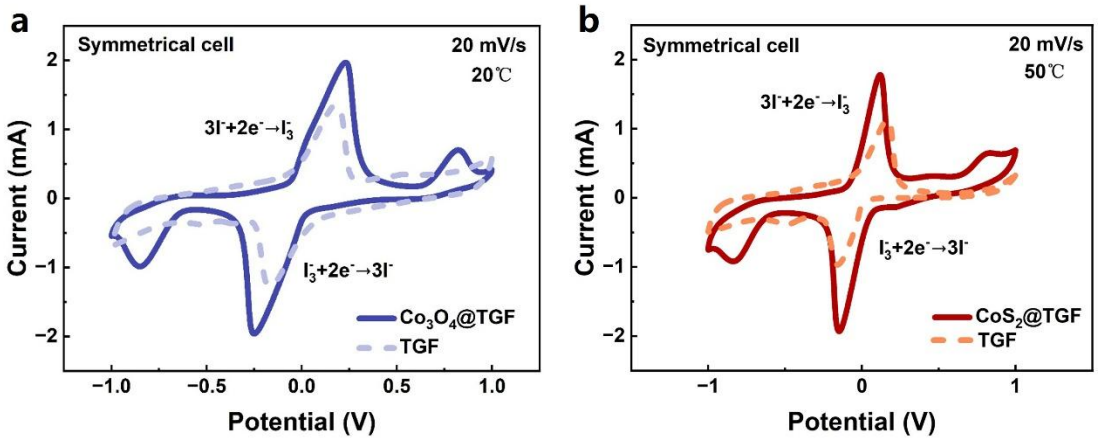

Fig. S5 Symmetric cell CV tests through a two-electrode system of (a) TGF-Co_3O_4@TGF and (b) TGF-CoS_2@TGF based on 0.01 M KI + 1 M KCl solution.

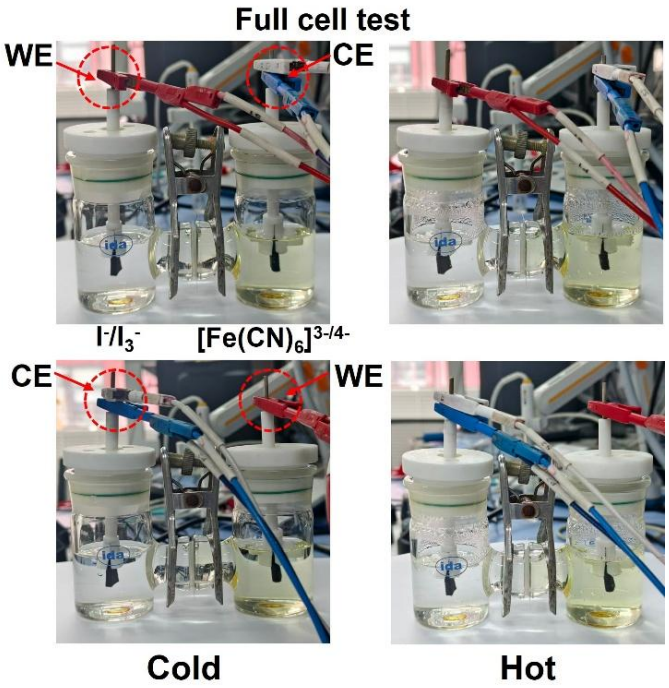

Fig. S6 Full cell tests through two-electrode system based on 0.01 M KI + 1 M KCl and 0.01 M $K_4Fe(CN)_6$ + 1 M KCl solution.

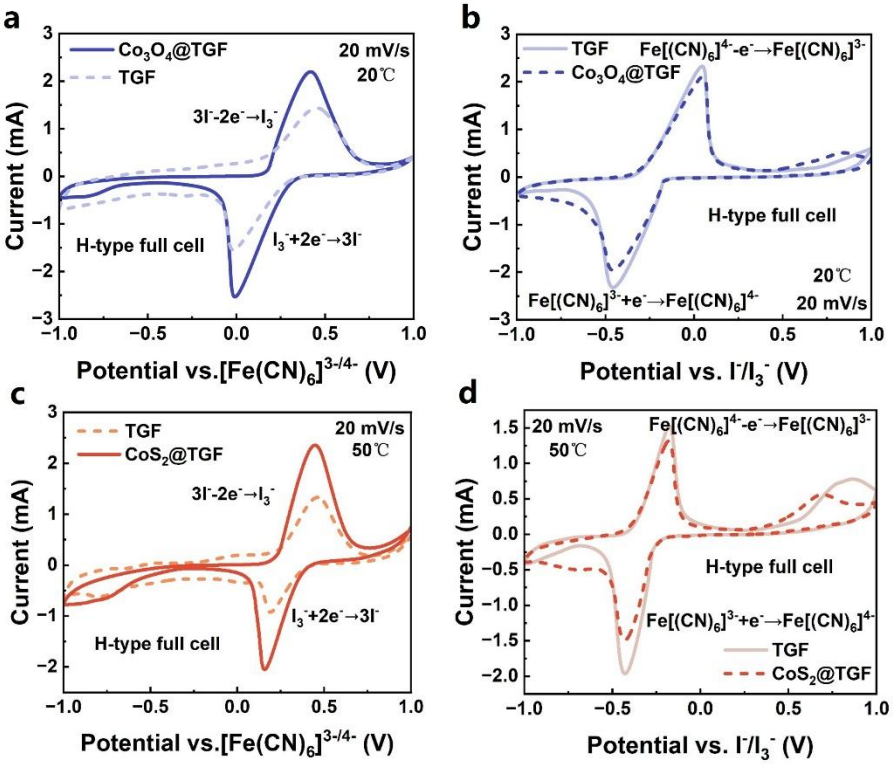

Fig. S7 (a) and (b) CV curves of TGF-Co_3O_4@TGF at 20ºC in a full cell test. (c) and (d) CV curves of TGF-CoS_2@TGF at 50ºC in a full cell test.

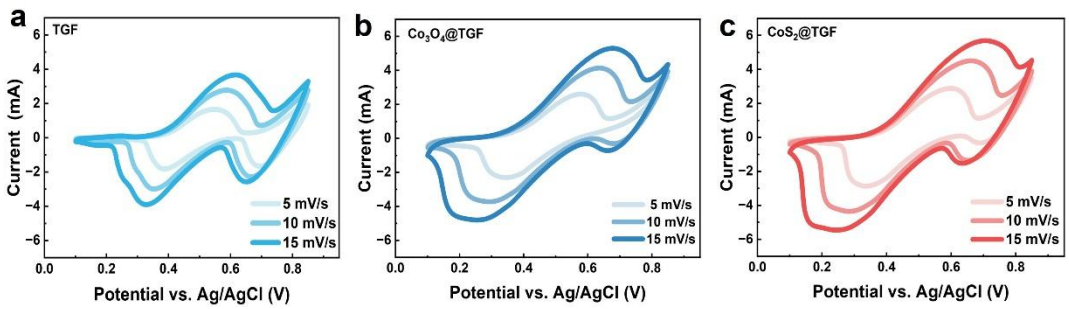

Fig. S8 CV curves under different scan rates in the three-electrode configuration based on (a) TGF. (b) Co_3O_4@TGF. and (c) CoS_2@TGF based on 0.01 M KI + 1 M KCl solution.

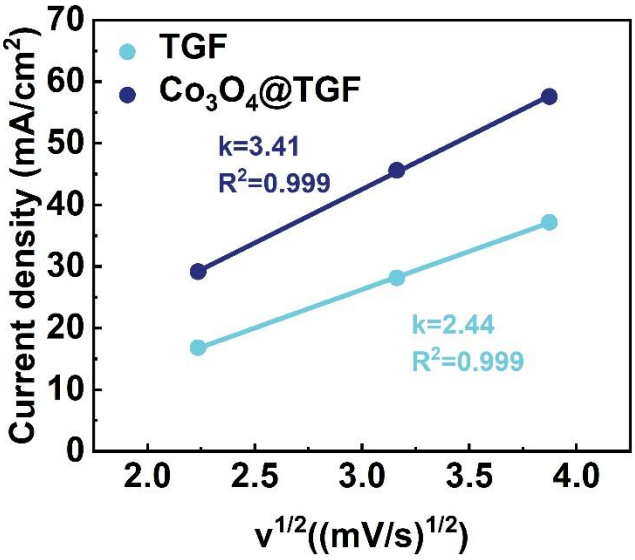

Fig. S9 The correspondence between peak current and the square root of scan rates.

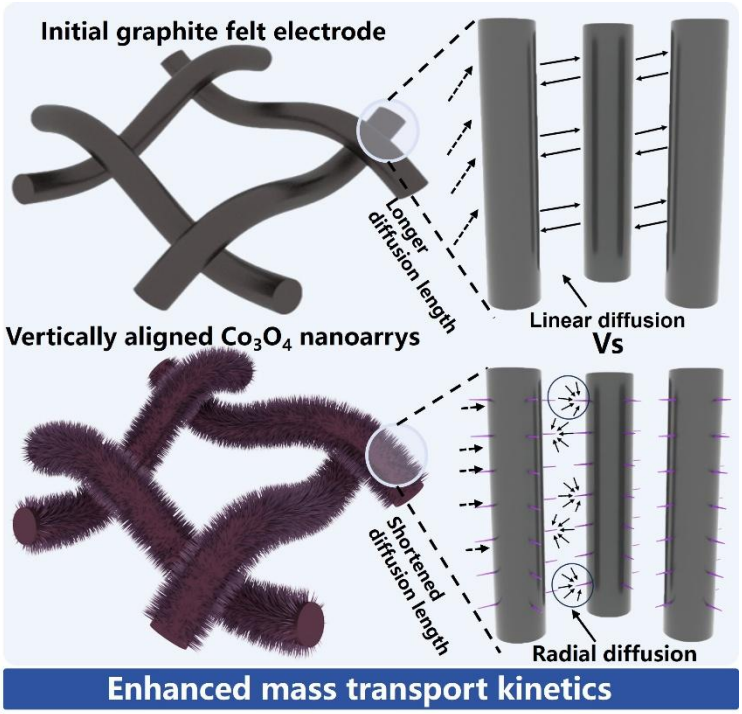

Fig. S10 Schematic diagram of mass transfer of active substances between Co_3O_4 nanoarrays.

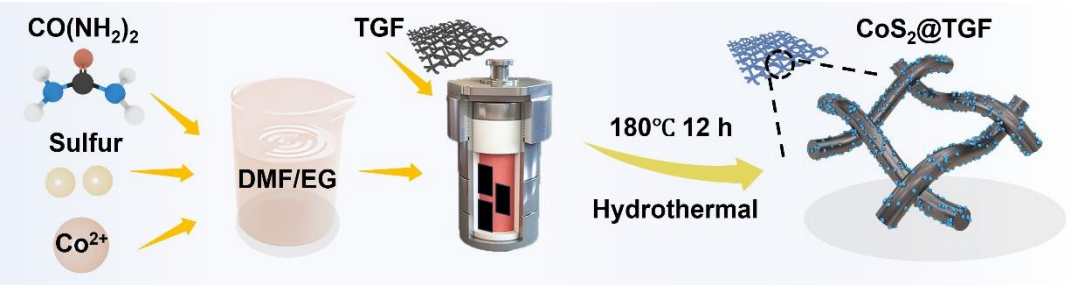

Fig. S11 Schematic process of CoS_2@TGF nanoarrays decorated with TGF by hydrothermal reaction.

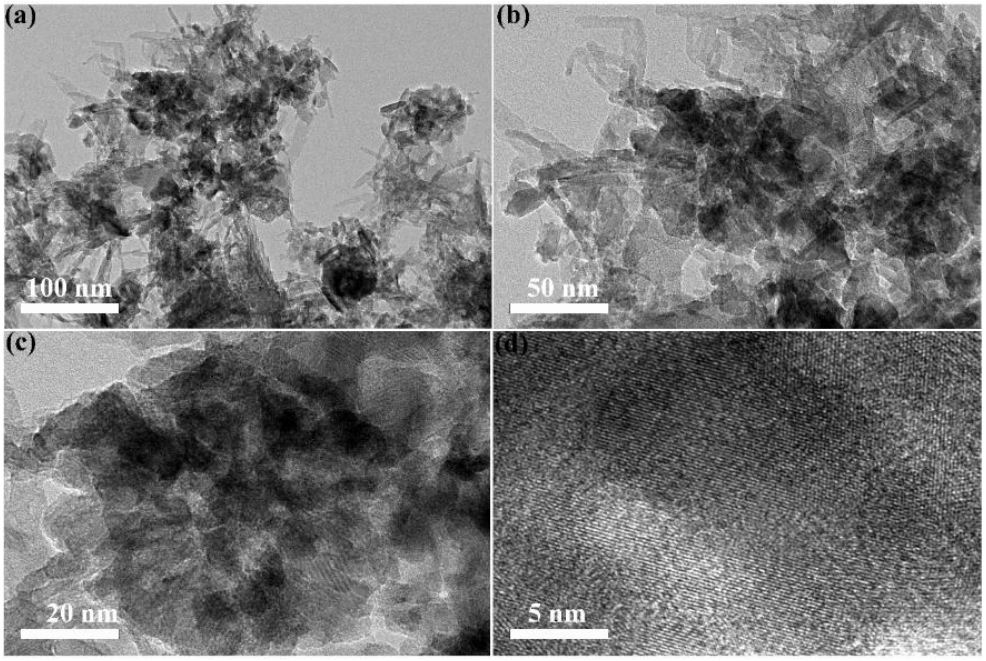

Fig. S12 (a)-(d) TEM photographs of CoS_2@TGF at different magnifications.

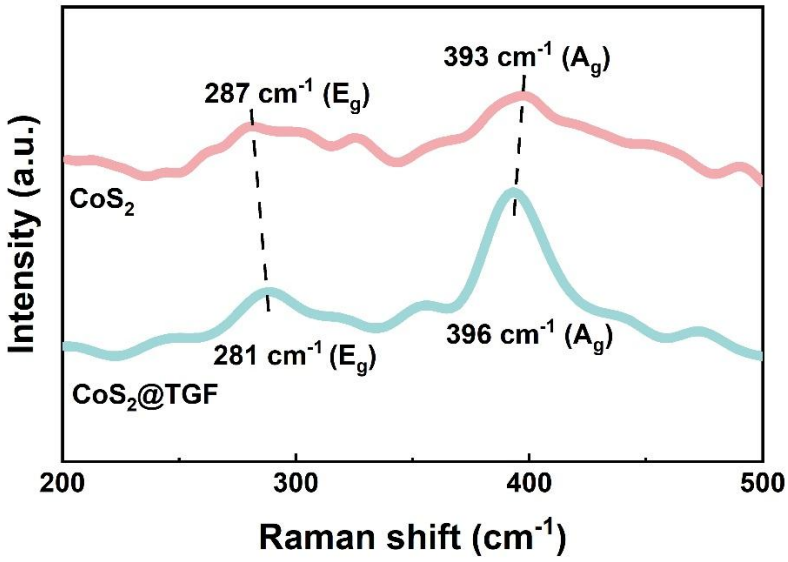

Fig. S13 Raman spectra of CoS_2 and CoS_2@TGF.

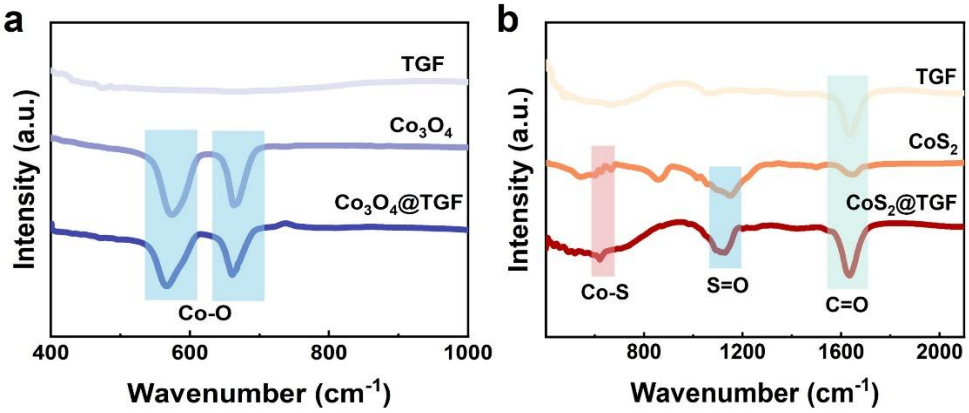

Fig. S14 Fourier Transform infrared spectroscopy (FTIR) of (a) Co_3O_4@TGF and (b) CoS_2@TGF.

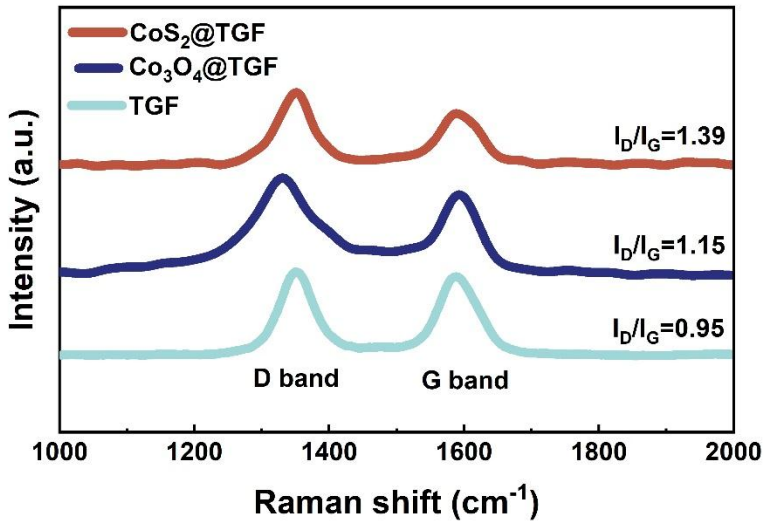

Fig. S15 Raman spectra of TGF, Co_3O_4@TGF, and CoS_2@TGF.

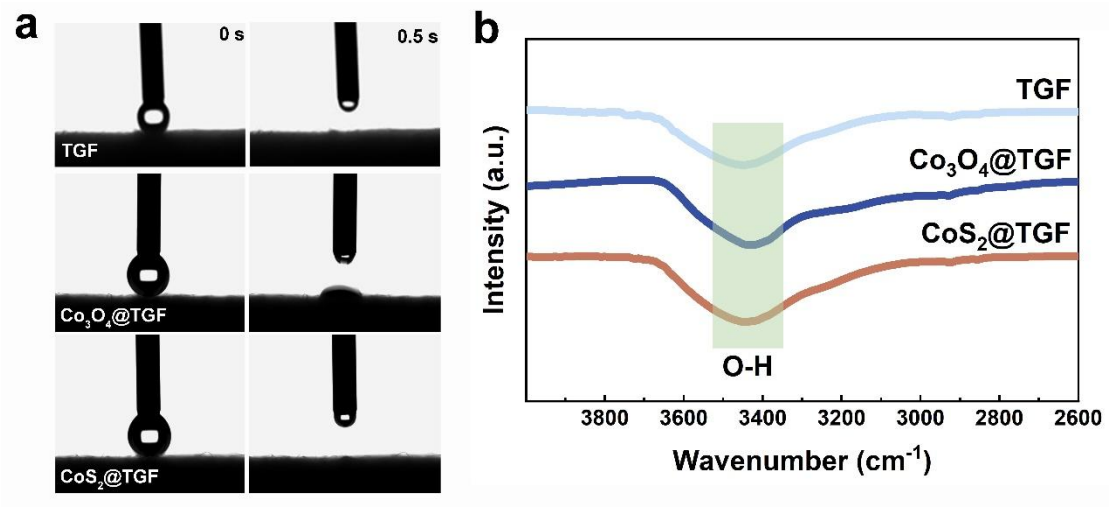

Fig. S16 (a) Contact angles and (b) FTIR of different electrode samples.

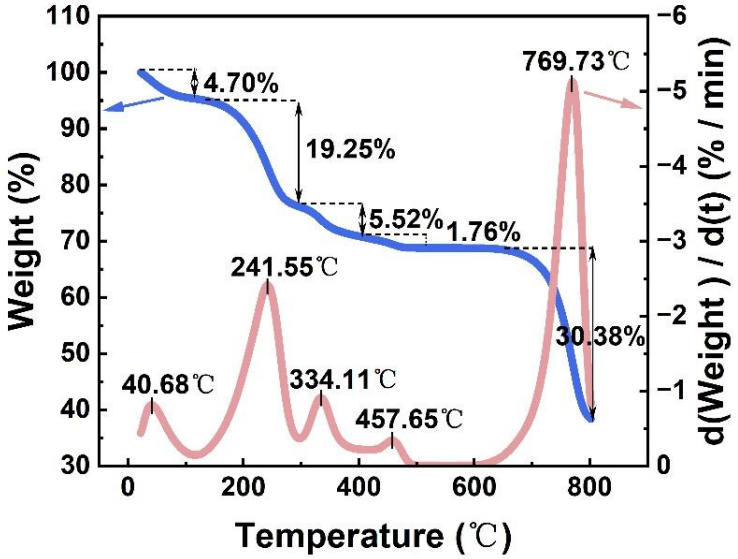

Fig. S17 Thermogravimetric Analysis (TGA) curve of CoS_2.

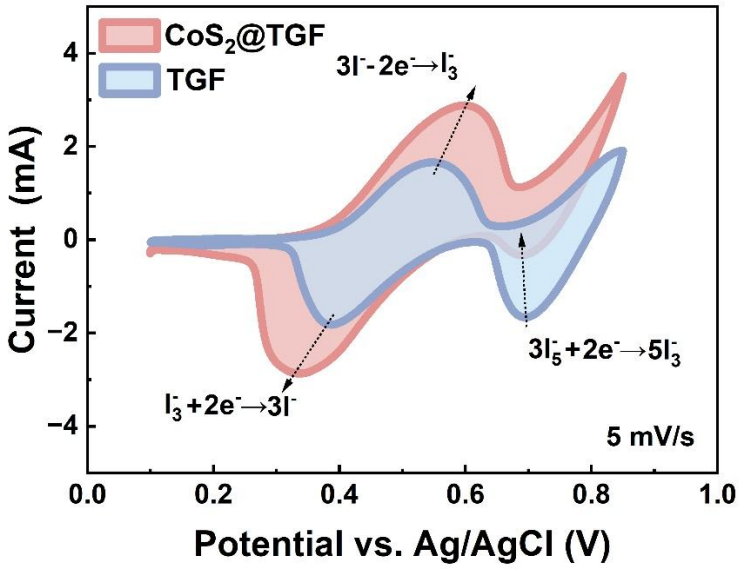

Fig. S18 CV curve of CoS_2@TGF and TGF under scan rate of 5 mV/s in the three-electrode configuration with the electrolyte of 10 mM KI + 1 M KCl.

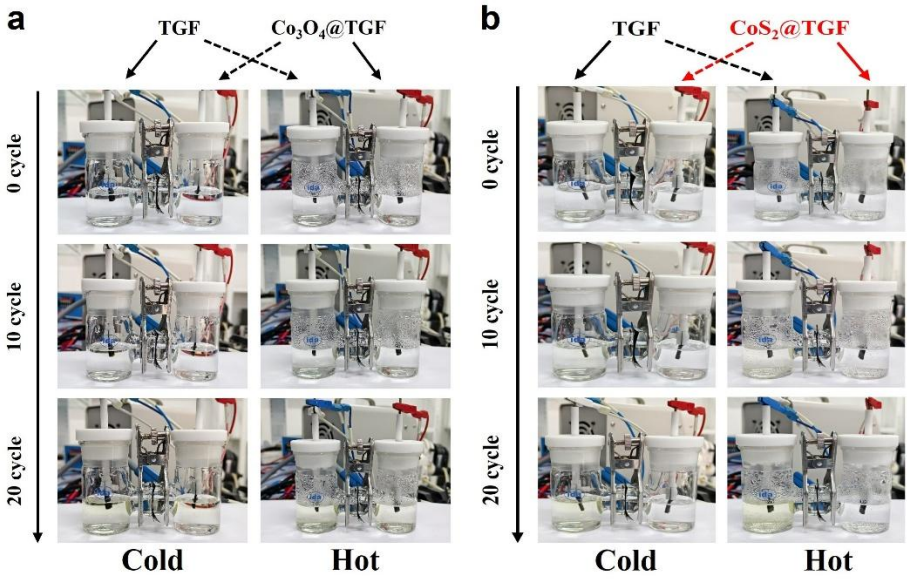

Fig. S19 Symmetric cell performance tests through a two-electrodes system of (a) TGF-Co_3O_4@TGF and (b) TGF-CoS_2@TGF.

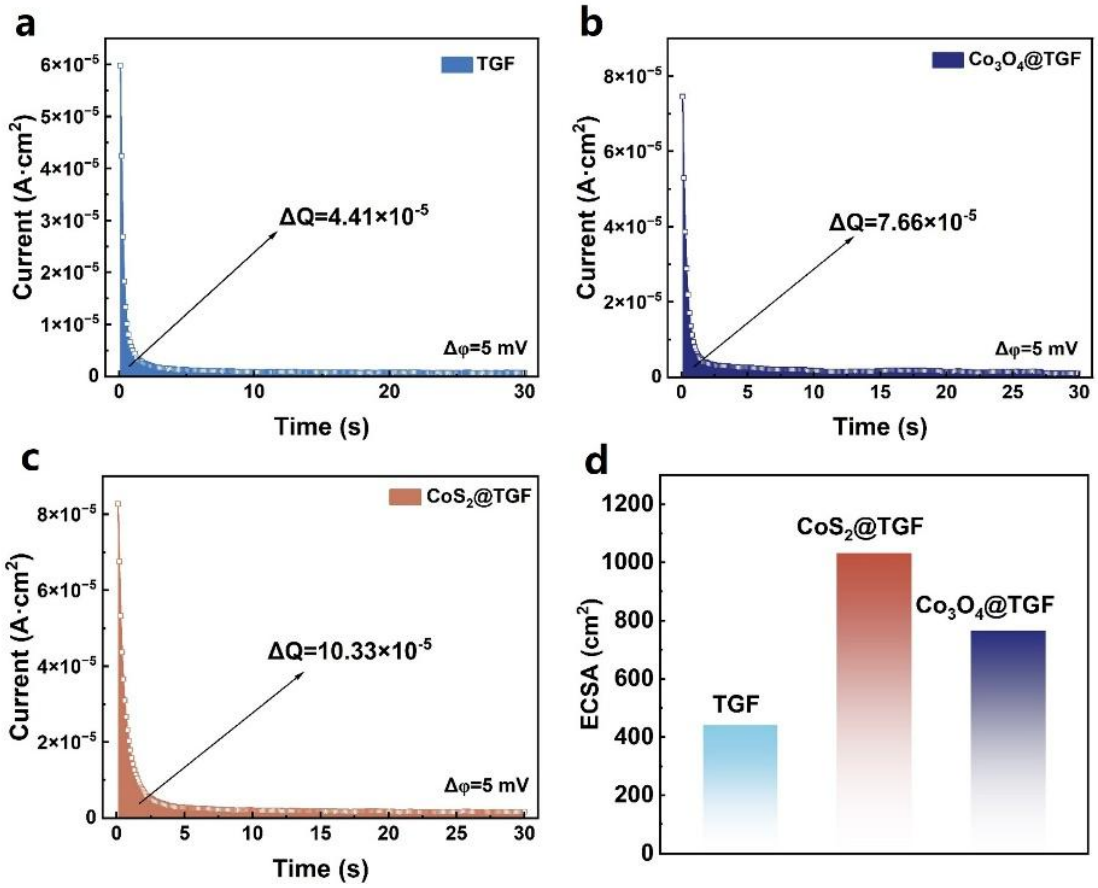

Fig. S20 Current-time (i-t) curve of (a) TGF, (b) Co_3O_4@TGF and (c) CoS_2@TGF. (d) Electrochemical specific surface area (ECSA) of different electrodes.

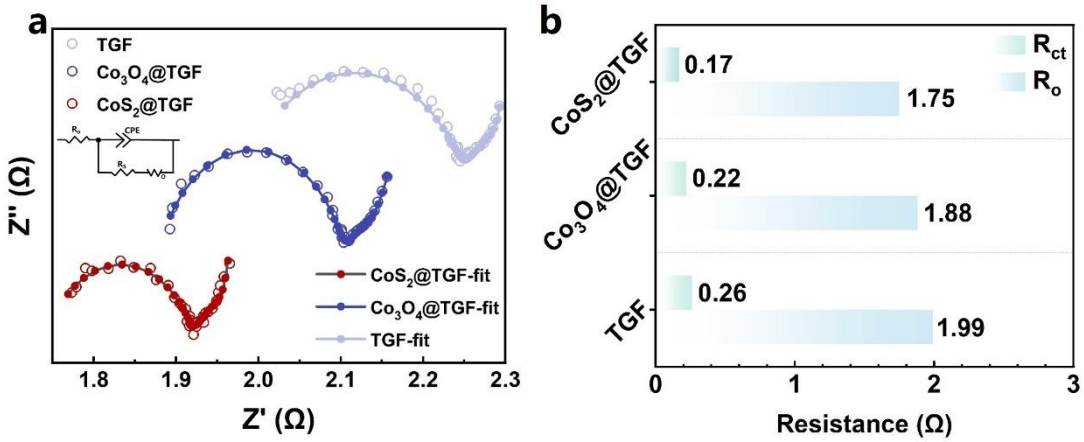

Fig. S21 (a) and (b) EIS spectra and corresponding DRT results of different electrode configurations in three-electrode system with electrolyte of 0.2 M I_2 + 0.6 M KI + 1 M KCl at room temperature.

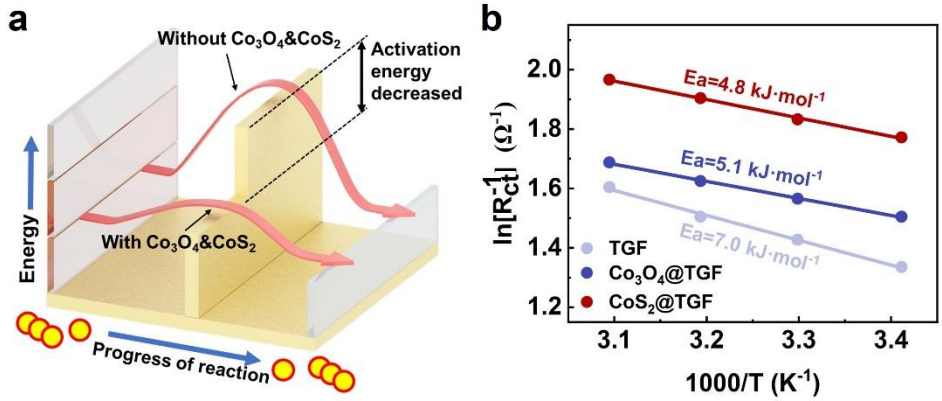

Fig. S22 (a) Schematic diagram of the influence of activation energy on the reaction process. (d) Activation energies of different electrodes during the I^-/I_3^- reaction process.

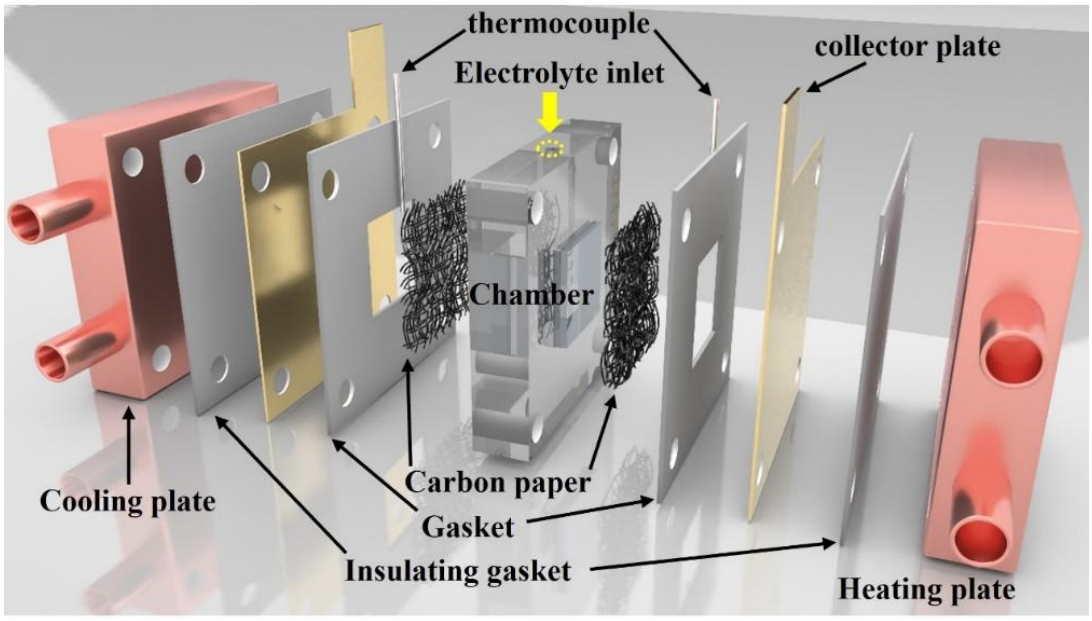

Fig. S23 Structural diagram for measuring TGC temperature coefficient.

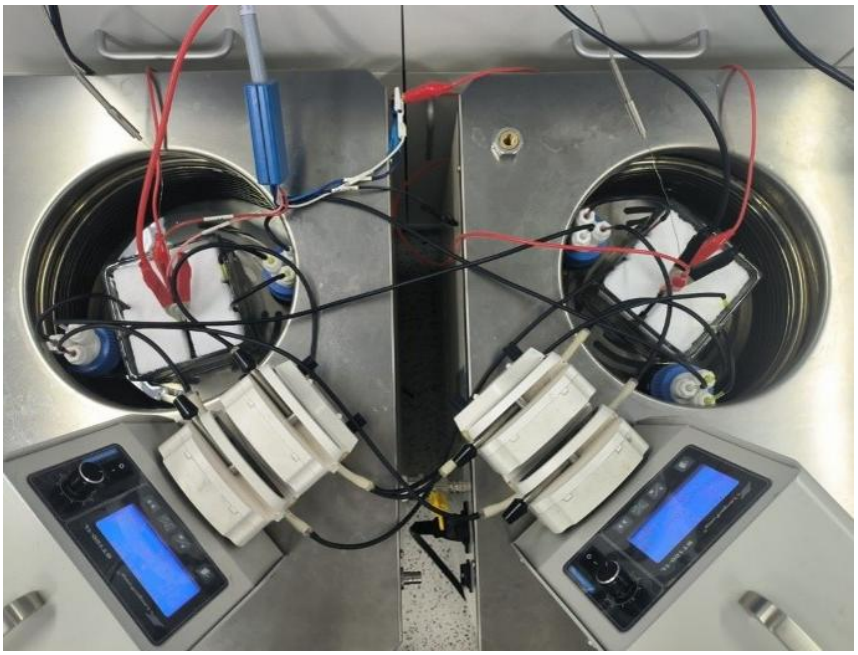

Fig. S24 Structure diagram of the TRFB device.

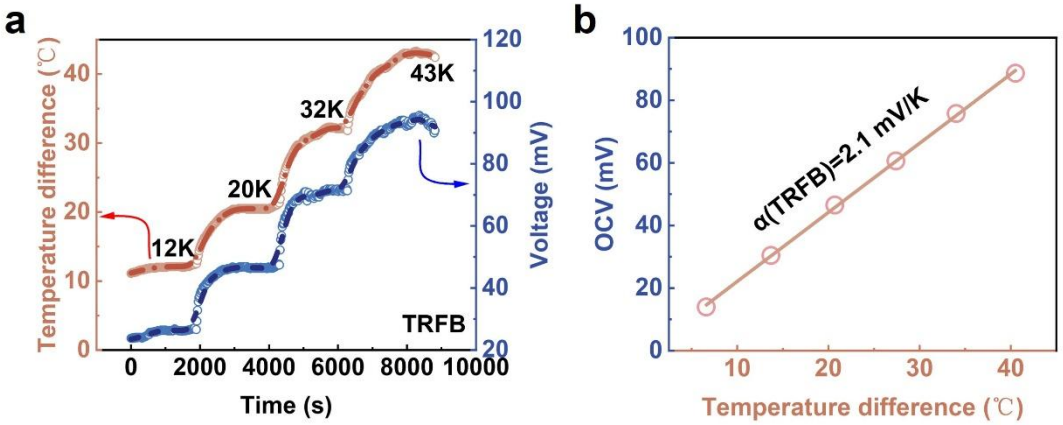

Fig. S25 (a) Variation of output voltage with temperature difference in the TRFB system.

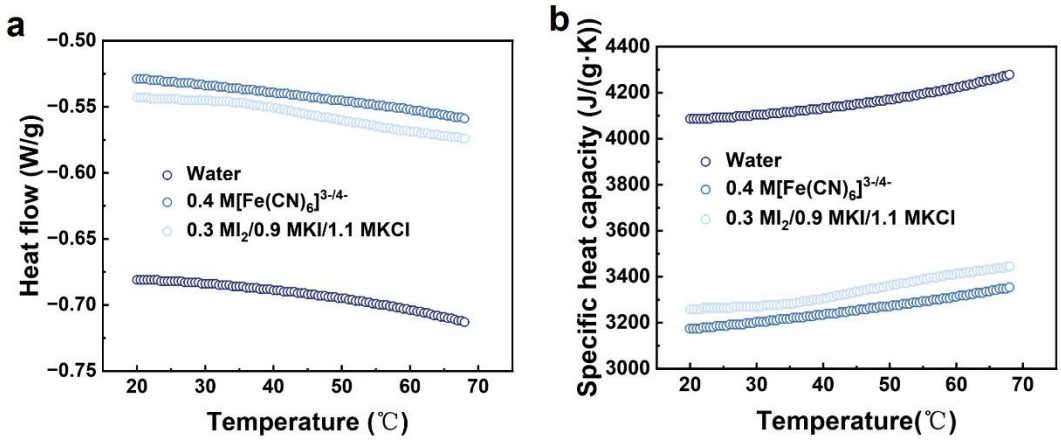

Fig. S26 (a) Differential scanning calorimetry (DSC) spectrum and (b) specific heat capacity curve of negative and positive electrolyte.

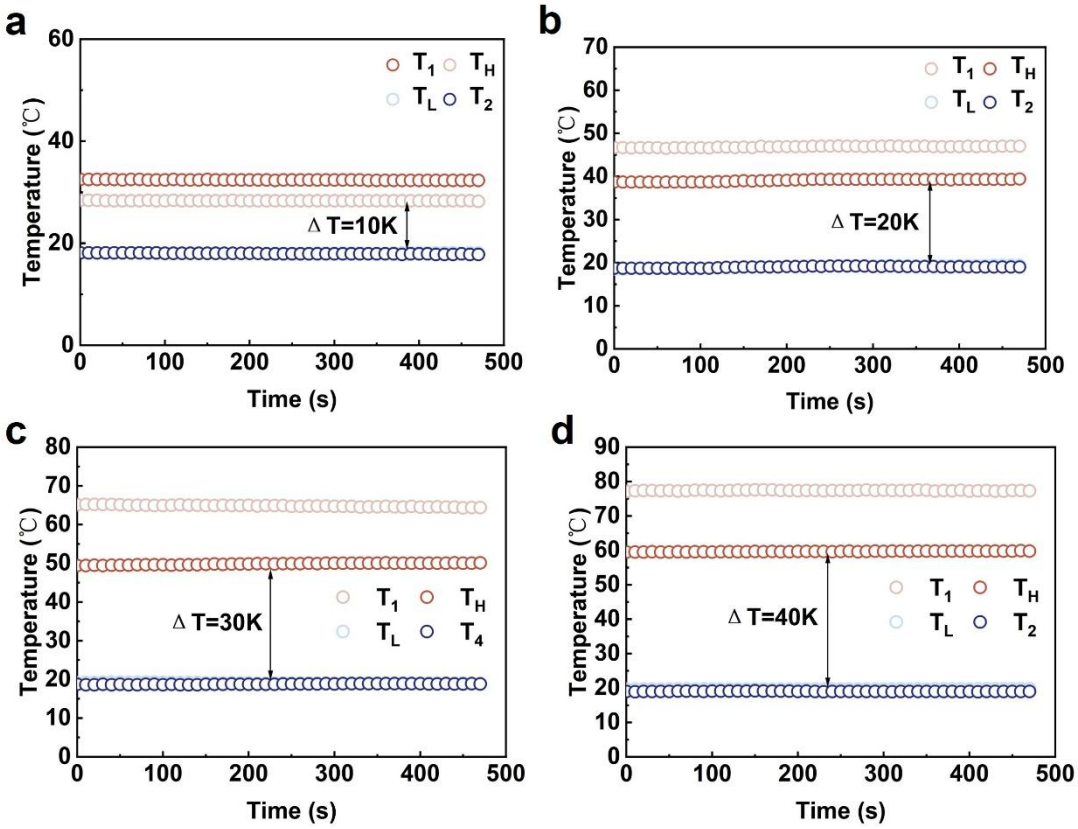

Fig. S27 The temperature distribution of the hot/cold source and hot/cold cell in the TRFB system under temperature differences of (a) 10K, (b) 20K, (c) 30K, and (d) 40K.

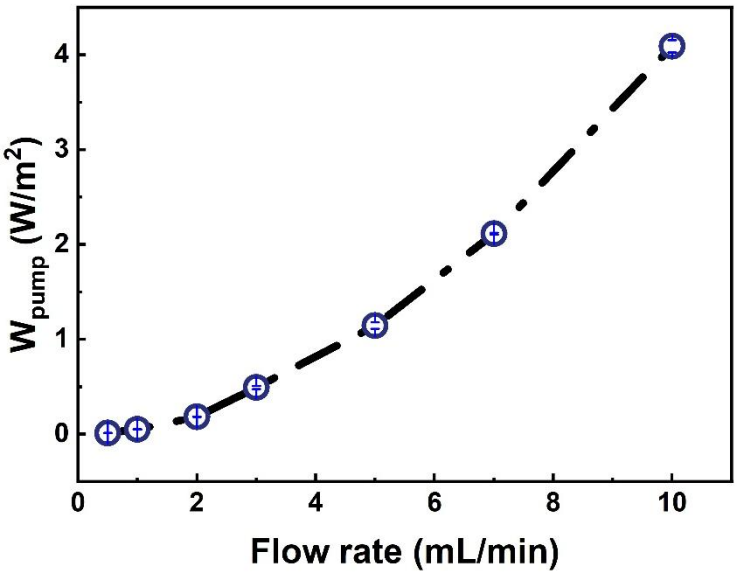

Fig. S28 Pump power consumption of TRFB at different electrolyte flow rates.

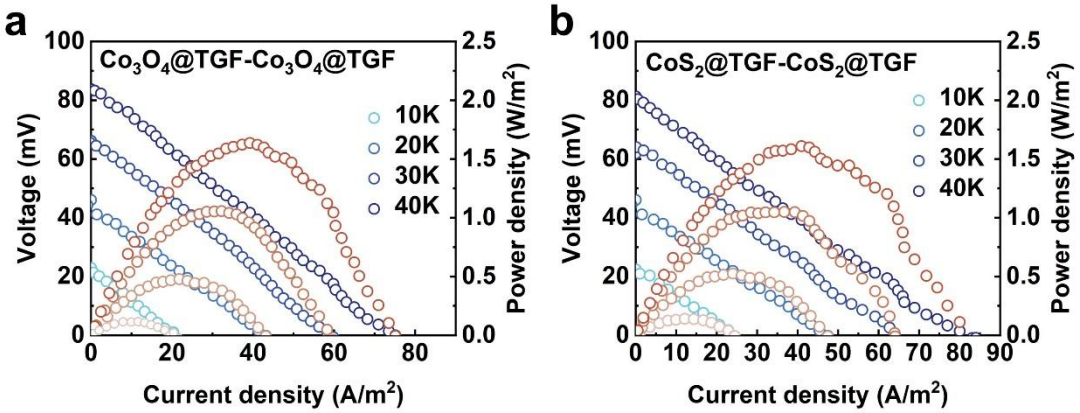

Fig. S29 Voltage-current density curve and power density curves of TRFB based on (a) symmetrical Co_3O_4@TGF-Co_3O_4@TGF electrodes and (b) asymmetric CoS_2@TGF-CoS_2@TGF electrodes.

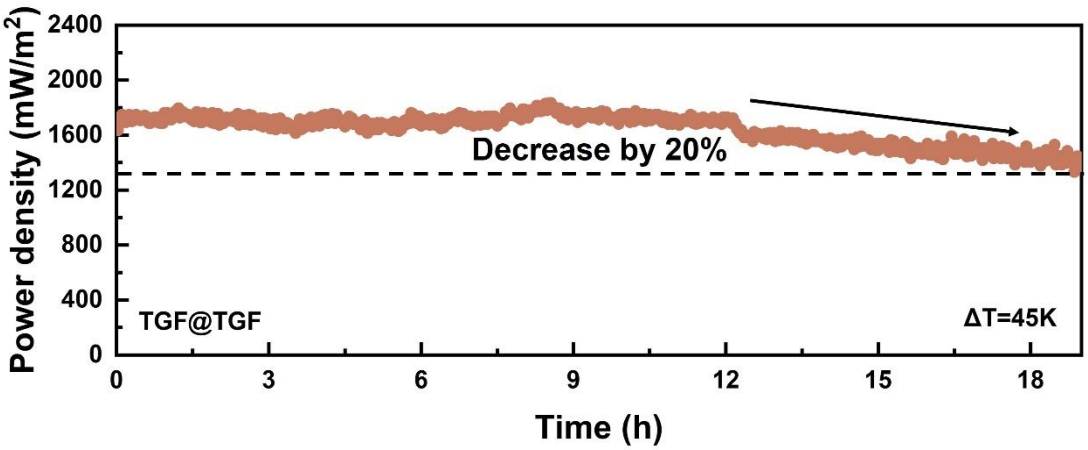

Fig. S30 Long-time operation of TRFB with TGF@TGF at ΔT of 45K.

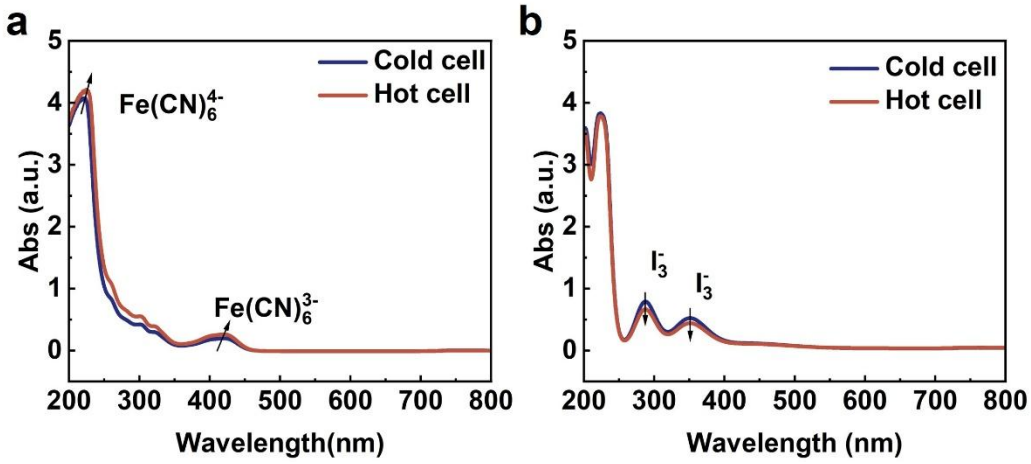

Fig. S31 Ultraviolet-visible spectra of electrolyte in hot and cold cell after long-term operation (a) $Fe[(CN)_6]^{3-/4-}$ and (b) I^-/I_3^-.

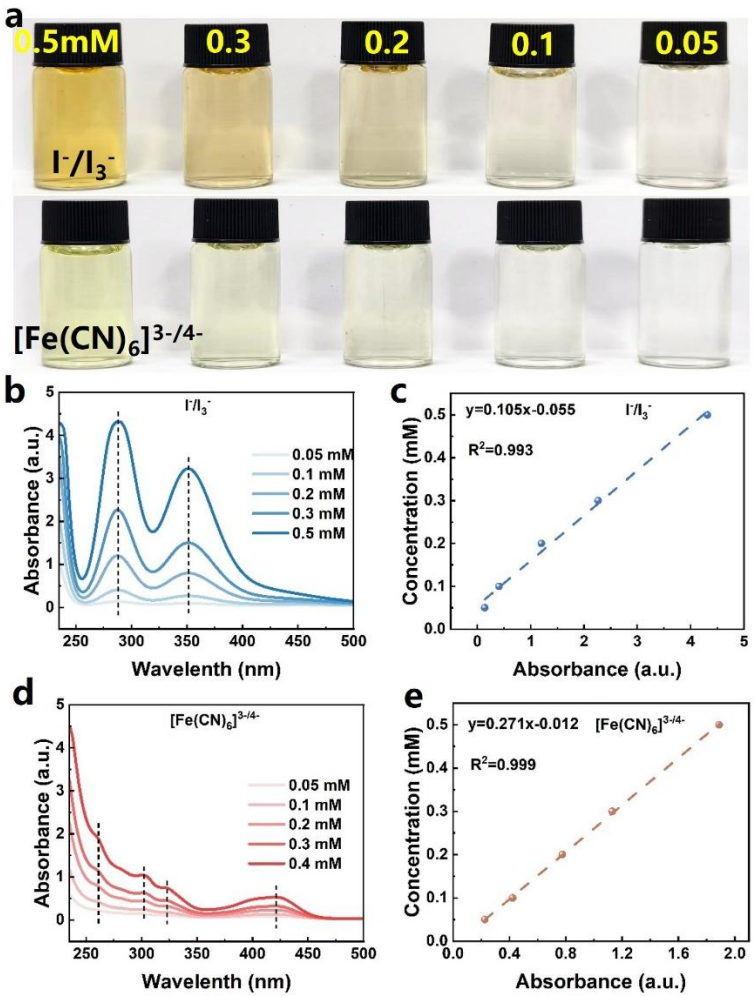

Fig. S32 (a) Pictures of solutions with different concentrations. (b) and (c) The UV-vis curves and relationship between absorbance and concentration of positive electrolyte at different concentrations. (d) and (e) The UV-vis curves and relationship between absorbance and concentration of negative electrolyte at different concentrations.

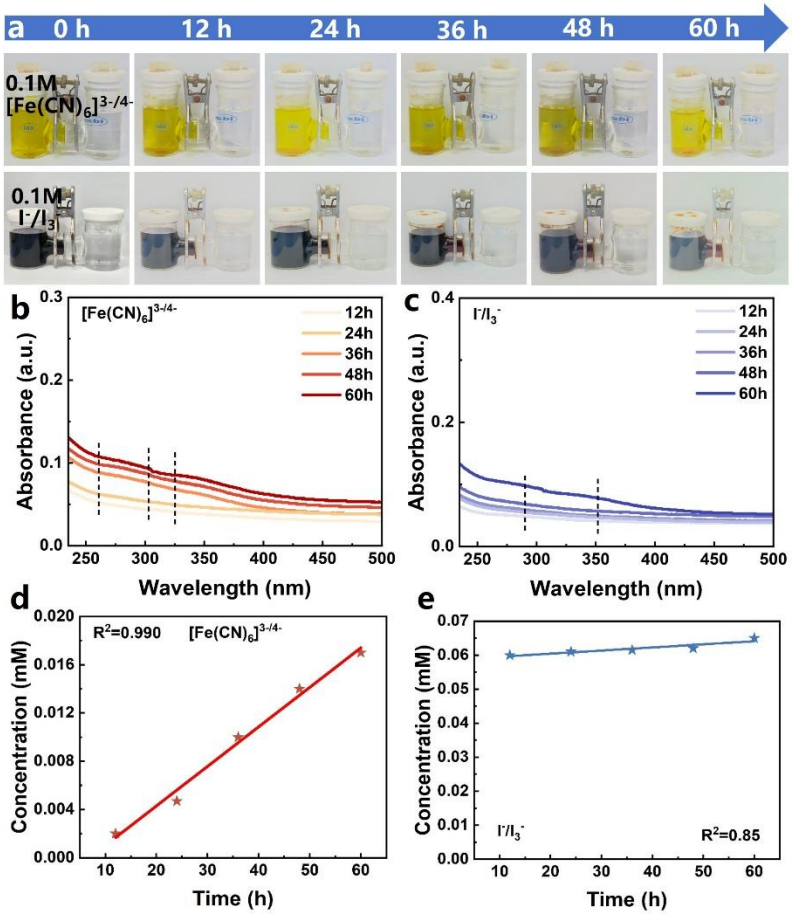

Fig. S33 (a) Pictures of crossover experiment of positive and negative active substances. The UV-vis curves corresponding to the crossover experiment of (b) negative electrolyte and (c) positive electrolyte. The relationship between diffusion time and concentration of (d) negative electrolyte and (e) positive electrolyte.

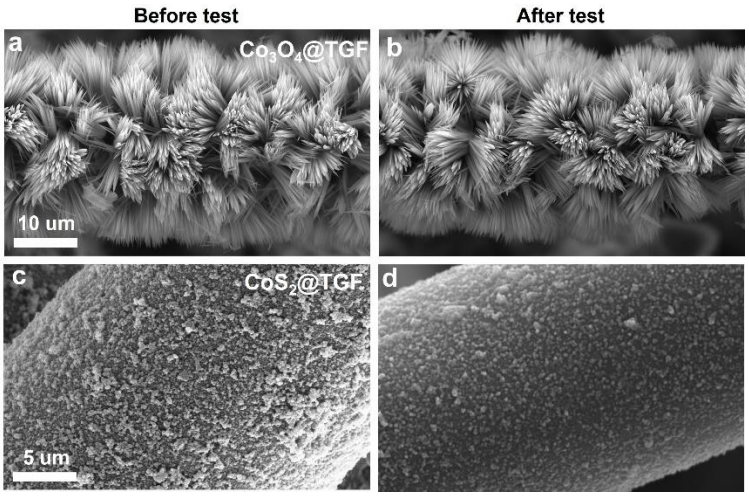

Fig. S34 SEM images before and after long-term running test of (a) and (b) Co_3O_4@TGF. (c) and (d) CoS_2@TGF.

Supplemental Tables

Table S1. The costs of different electrodes with the size of 1 cm×1 cm×0.3 cm.

Electrode	Raw material	Weight (g)/Area(cm^2)	Price ($/g)/($/cm^2)	Total price ($)
Co_3O_4	$Co(NO_3)_2·6H_2O$	0.048	0.047	0.014
	Urea	0.015	0.007	
	NH_4F	0.0031	0.014	
	TGF	1	0.0042	
CoS_2	$CoSO_4·7H_2O$	0.023	0.044	0.006
	Urea	0.025	0.007	
	Sulfur	0.017	0.02	
	TGF	1	0.0042	
Pt/C	Pt/C(1mg/cm^2)	1	0.9	0.9

Table S2. Cost calculations of the TRFB system with electrode size of 1 cm ×1 cm

	Electrolyte cost ($)	Electrode cost ($)	Membrane cost ($)	Power density (W/m^2)	CPM ($/(W/m^2))
Our work	0.2MI^-/I_3^-+1MKCl 0.2MFe$[(CN)_6]^{3-/4-}$ 0.45	Co_3O_4 CoS_2 0.0404	Nafion212 0.7	2.30	0.52
Ref.1	1M$V^{2+/3+}$+6MHCl 0.375M$[Fe(CN)_6]^{3-/4-}$ 1.5	Carbon paper 0.17	Nafion212 0.7	1.40	1.69
Ref.2	0.1MI^-/I_3^-+1MKI 0.375M$[Fe(CN)_6]^{3-/4-}$ 0.65	Graphite felt 0.0168	Nafion212 0.7	0.14	9.76
Ref.3	0.3MI^-/I_3^-+1.1MKCl 0.3M$[Fe(CN)_6]^{3-/4-}$ +0.35MKCl 0.75	Graphite sheet 0.056	Nafion212 0.7	1.05	1.43

Table S3. Performance comparison of different thermoelectric conversion systems

Systems	Electrode/electrolyte	T_L-T_H (°C)	α (mV/K)	η_r (%)	Power density ($mW \cdot m^{-2} \cdot K^{-2}$)	Ref.
TRFB	Electrode:Graphite felt Electrolyte:0.2MI^-/I_3^-+1MKCl/0.2M$[Fe(CN)_6]^{3-/4-}$	20-60	2.02	4.7	1.41	This work
	Electrode: Carbon paper+Pt/C Electrolyte:1M $V^{2+/3+}$+6MHCl/0.375M$[Fe(CN)_6]^{3-/4-}$	10-50	3	1.86	0.69	1
	Electrode:Graphite felt Electrolyte:0.1MI^-/I_3^-+1MKI/0.375M$[Fe(CN)_6]^{3-/4-}$	20-60	1.9	9	0.07	2
	Electrode:Graphite sheet Electrolyte:0.3MI^-/I_3^-+1.1MKCl/0.3M$[Fe(CN)_6]^{3-/4-}$+0.35MKCl	20-80	2.88	/	0.52	3
	Electrode:Graphite felt Electrolyte:0.01MI^-/I_3^-+1.2MKI+0.1M$CcCO_2$/ML	10-50	2.85	6	0.02	4
TREC	Electrode:PB/CF Electrolyte:2.5MKNO_3/0.3M$[Fe(CN)_6]^{3-/4-}$	20-60	1.4	4.33	0.09	5
	Electrode:RGO/CF Electrolyte:0.1MI^-/I_3^-+2MKI/0.5M/0.1M$[Fe(CN)_6]^{3-/4-}$	30-65	1.8	11.9	0.27	6
TGC	Electrode:Graphite plate Electrolyte:$[Fe(CN)_6]^{3-/4-}$+GdmCl	20-70	3.73	11.1	7.08	7
	Electrode:Graphite plate Electrolyte:$[Fe(CN)_6]^{3-/4-}$+GdmCl+Urea	20-30	4.2	0.79	1.1	8
	Electrode:Fe-N-C+Carbon cloth Electrolyte:0.8M$Fe(ClO_4)^{2+/3+}$	20-50	1.64	0.56	/	9
	Electrode:Mxene-HM+SWCNTs Electrolyte:0.1M$Fe^{2+/3+}$+HCl	20-60	1.2	/	0.53	10

Supplemental Notes

Note S1: Techno-economic analysis

The use of earth-abundant non-precious metal Co_3O_4 and CoS_2 catalysts significantly reduces the electrode material cost compared with noble metal-based electrodes. Furthermore, the doubled normalized power density allows for a nearly 30% reduction in the required stack size and membrane area for a given target power output, which are the main cost drivers of TRFB systems, thus greatly improving the overall system economics.[11] The simple in-situ hydrothermal preparation process is compatible with industrial production, further ensuring the economic viability of large-scale application.

Note S2: Robustness and scalability of the electrodes

The robust chemical bonding between the in-situ grown catalysts and the TGF substrate ensures excellent mechanical and structural stability under continuous electrolyte flow and thermal cycling, as evidenced by the 70-hour stable operation and post-mortem microscopic and spectroscopic analysis. The simple, low-cost hydrothermal preparation process using earth-abundant raw materials endows the electrodes with excellent scalability,[12] which is compatible with the existing industrial production of flow battery electrodes and stack assembly.

Note S3: Mott-Schottky Analysis

Mott-Schottky analysis is a standard electrochemical technique for characterizing the semiconductor properties of electrode materials. The Mott-Schottky analysis characterize the semiconductor-electrolyte interface by measuring the space-charge capacitance (C_S) against applied potential according to the Mott-Schottky equation [13]:

$$C_S^{-2} = \frac{2}{\varepsilon\varepsilon_0 e N_D}(E - E_{fb} - \frac{kT}{e}), n-type$$

$$C_S^{-2} = -\frac{2}{\varepsilon\varepsilon_0 e N_A}(E - E_{fb} - \frac{kT}{e}), p-type$$

Where, E_{fb} is the uniform electric potential, N_D and N_A are the carrier concentrations, ε is the relative dielectric constant, ε_0 is the vacuum dielectric constant, k is the Boltzmann constant, T is the absolute temperature, and e is the unit charge quantity. Evaluating the relationship between $1/C_s^2$ and the applied potential, we can determine three key parameters of the semiconductor: (1) The semiconductor type is identified by the sign of the slope in the linear region, with a negative slope indicating a P-type semiconductor and a positive slope indicating an N-type semiconductor. (2) The flat-band potential (E_{fb}) extracted from the x-axis intercept, which is essential for analyzing band bending and charge transfer at the semiconductor-electrolyte interface. (3) The carrier concentration can be directly calculated from the slope of the linear region, which is inversely proportional to the magnitude of the slope.

A fixed-frequency alternating disturbance signal (with the alternating frequency typically ranging from 1 to 20 kHz) is applied. The impedance values at different potentials are measured, and the depletion region capacitance C_S is calculated based on

the imaginary part of the impedance.

$$C_S = -1/\left(2\pi f * Im(Z)\right)$$

Where C_S is the space charge capacitance, *f* is the frequency, lm(Z) is the imaginary part of electrical impedance (Z). Experimentally, these measurements were meticulously executed using a Biologic VSP-300 Electrochemical Workstation operating in a standard three-electrode configuration. We utilized a 1 cm × 1 cm Co_3O_4@TGF or CoS_2@TGF working electrode, an Ag/AgCl (saturated KCl) reference electrode, and a platinum mesh counter electrode. The tests were performed utilizing the Staircase Potentio Electrochemical Impedance Spectroscopy technique in a neutral 0.5 M Na_2SO_4 aqueous solution at scanning frequencies of 1000 Hz, 1468 Hz, and 2154 Hz.

Note S4: Electrochemical Active Surface Area measurement

The Electrochemical Active Surface Area measurement (ECSA) of the porous felt used in this study was determined by chronoamperometry technique in three electrode system, in which the constant potential was set in 5 mV vs open-circuit potential (OCV) and the 1 M KCl was used as the electrolyte. The integral of the obtained i-t curve was calculated to access the ECSA of prepared samples. In the test, a small constant potential Δφ (5 mV) is applied on the open circuit potential to charge the electric double layer, the current is recorded as the function of time. The calculation formulas for SSA are listed as follows:[14]

$$C_d = \Delta Q / \Delta \varphi$$

$$ECSA = C_d / \left(20\mu F \cdot cm^{-2}\right)$$

where ΔQ is charge capacity of electric double layer, which is obtained through the integral of the i-t curve. $\Delta\varphi$ is 5 mV. The C_d of mercury smooth surface is 20 $\mu F \cdot cm^{-2}$. which is the standard reference value for carbon-based electrodes in aqueous electrolytes.[15]

Supplemental Experimental Procedures

Chemicals and materials preparation

Materials

All reagents were used exactly as received. Potassium ferricyanide ($K_3Fe(CN)_6$, <99%), Potassium ferrocyanide trihydrate ($K_4Fe(CN)_6 \cdot 3H_2O$, >99%), Iodine (I_2, >99.8%), Potassium iodide (KI, >99%), Ammonium fluoride (NH_4F, >99%) Sublimed sulfur (S, >99.5%), Cobaltous nitrate hexahydrate ($Co(NO_3)_2 \cdot 6H_2O$, >99%) Cobalt sulfate heptahydrate ($CoSO_4 \cdot 7H_2O$, >99%), Urea (>99.5%), N, N-Dimethylformamide (DMF, >99%) and Ethylene glycol (EG, >99.8%) were purchased from Shanghai Aladdin Bio-Chem Technology Co., LTD. Nafion membrane (N212) was bought from Sinero Energy Store. The electrolyte was prepared using deionized (DI) water.

Preparation of Co_3O_4@TGF electrode for the cold cell of TRFB

Co_3O_4 was synthesized using a one-step hydrothermal method and low-temperature annealing. Mix 0.58 g $Co(NO_3)_2 \cdot 6H_2O$, 0.18 g mmol urea, and 0.037 g NH_4F in 40 mL DI. Place TGF (1 cm × 1 cm × 3 mm) in the precursor solution, then transfer it to a 50 ml high-pressure reactor lined with Teflon, maintain the reaction

temperature at 120℃ for 6 hours, and finally dry under vacuum at 60℃ for 12 hours to obtain $Co(OH)_x{\cdot}H_2O$. Place the obtained $Co(OH)_x{\cdot}H_2O$ in a tube furnace, anneal at 300℃ and N_2 atmosphere for 2 hours, and finally collect Co_3O_4-O_V@TGF Electrode. The $Co(OH)_x \cdot H_2O$ was annealed in a muffle furnace at 300℃ for 2 hours in an air atmosphere to obtain Co_3O_4@TGF.

Preparation of CoS_2@TGF electrode for the hot cell of TRFB

The GF was first ultrasonically cleaned several times and then heat-treated at 500°C for 5 h to obtain TGF. The CoS_2 was synthesized by a hydrothermal approach. Specifically, 0.2811 g of $CoSO_4{\cdot}7H_2O$, 0.3 g of urea, and 0.2 g of sulfur were mixed in a 35 mL solution of EG: DMF=9:10. The precursor solution was magnetically stirred until a uniform suspension was formed and subsequently transferred into a 50 mL Teflon-lined autoclave. The autoclave was placed at 180°C for 12 h. The product was collected by centrifugation, washed several times with DI water and absolute ethanol, and dried at 60°C for 12 h. To prepare the CoS_2@TGF electrode, the TGF (1 cm × 1 cm × 3 mm) was placed in the precursor solution, and the remaining conditions are the same as the above steps. Finally, the TGF loaded with CoS_2 was washed several times with DI water and dried at 60°C for 12 h to obtain CoS_2@TGF.

Configuration of the TGC system

In terms of electrode size, the working and counter electrodes used in the TGC are both heat-treated carbon paper, with an effective geometric area of 2.5 cm × 2.5 cm and a thickness of 0.2 mm. The inter-electrode distance, specifically the distance between the working electrode (hot end) and the counter electrode (cold end), is 1 cm. For the

electrolyte chamber, the cell is clamped with polytetrafluoroethylene (PTFE) that has a size of 6 cm × 6 cm × 1 cm, and each electrode is placed in a PTFE electrolyte chamber with an internal volume of 4 mL. To prevent electrolyte leakage, a fluorine rubber gasket with a thickness of 0.5 mm is used between the electrode and the chamber. As for the current collector, graphite bipolar plates with a size of 6 cm × 6 cm × 0.1 cm are adopted, which are in close contact with the back of the electrode to ensure good electrical conductivity. In terms of temperature control, the water-cooled copper plates are connected to a temperature-controlled water bath, with the cold end maintained at 20°C and the hot end heated in a gradient from 20°C to 50°C.

Configuration of the TRFB system

The dimensions of the TRFB system are detailed as follows: In terms of the active electrode area, the geometric area of the working electrode is 1 cm × 1 cm. Regarding the electrode thickness, the TGF-based electrode has a thickness of 3 mm in the original state and is compressed to 2 mm during cell assembly. For the electrolyte chamber volume, each half-cell (cold cell and hot cell) has a volume of 0.2 mL. The inter-electrode distance between the positive and negative electrodes in each half-cell is 0 mm, with the two electrodes separated by a Nafion 212 cation exchange membrane (2.5 cm × 2.5 cm). As for the bipolar plate, a graphite bipolar plate with a size of 4 cm × 5 cm × 0.1 cm is adopted. The cell housing is clamped with PTFE of 8 cm × 8 cm × 1 cm, which also provides thermal insulation for the cold and hot cells. Peristaltic pumps (Model: Langer Pump BT100-1L) were used to circulate the electrolyte in the cold and hot cells respectively, with one pump allocated to each half-cell. Silicone tubing with

an inner diameter of 1.6 mm and an outer diameter of 3.1 mm was used for the electrolyte circulation loop. The electrolyte flow rate was optimized at 74 μL/min for all experiments, a value that balances mass transport and pump power consumption. For the electrolyte tanks, glass reagent bottles with a volume of 50 mL were used as the electrolyte reservoirs for the cold and hot cells respectively. Regarding the temperature control system, the cold cell and its electrolyte reservoir were placed in a low-temperature constant-temperature reaction bath (Model: DFY-10/30), maintained at 20°C for all experiments; meanwhile, the hot cell and its electrolyte tank were placed in another low-temperature constant-temperature reaction bath, with the temperature varied from 30°C to 60°C to achieve different temperature differences (ΔT). Two K-type thermocouples were inserted into the electrolyte inlet of each half-cell to monitor the actual temperature of the electrolyte entering the cell in real time, and the temperature data was recorded by a portable paperless recorder (GP20, Yokogawa).

Electrochemical Characterization

CV, CA and EIS were operated using a three-electrode system and electrochemical workstation (Biologic VSP-300, France) at room temperature. The TGF, CoS@TGF and CoS_2@TGF were utilized as working electrodes. A Pt mesh and Ag/AgCl were used as the counter and reference electrodes, respectively. The CV curves were measured from 0.1 to 0.85 V versus Ag/AgCl in 10 mM KI as redox specie and 0.5 M KCl as the supporting electrolyte with a scan rate of 5, 10 and 15 $mV \cdot s^{-1}$ at room temperature. The Electrochemical specific surface area (ECSA) was measured by CA method in three electrode system, in which the constant potential was set in 5 mV vs

open-circuit potential (OCV) and the 0.5 M KCl was used as the electrolyte. The integral of the obtained i-t curve was calculated to access the ECSA of prepared samples. The LSV curves were operated using a three-electrode system and electrochemical workstation (Biologic VSP-300, France) at different temperature differences (10K, 20K, 30K and 40K). LSV curves were obtained at a scan rate of 0.1 $mV \cdot s^{-1}$. J_{sc} was measured from a range of OCV to 0 V in TRFB. EIS was conducted in 0.1 M I^-/I_3^- electrolyte at voltage of OCV with frequency range from 100 kHz to 0.01 Hz and amplitude of 5 mV.

Temperature coefficient measurement

For TGC, the Seebeck coefficient is calculated by measuring the voltage difference in response to the temperature difference. Use a digital multimeter (DMM 6500, Tektronix, America) to measure the potential difference between the two electrodes. For TRFB, we characterized the open-circuit voltage and its variation with the temperature difference between the cold and hot cells. The negative collectors of the two cells $[Fe(CN)_6]^{3-/4-}$ were connected by wires, the positive collector of the hot cell I^-/I_3^- served as the working electrode, and the other positive of the cold cell was used as the counter electrode and reference electrode. Use a digital multimeter (DMM 6500, Tektronix, America) to measure the potential difference between the two cells. Furthermore, the temperature coefficient of the electrode/ electrolyte can be determined by comparing the equilibrium potential of the tested electrode/electrolyte within the temperature range of 25°C with that of the Ag/AgCl reference electrode in a saturated potassium chloride aqueous solution.[16]

Characterization

The morphologies of all samples were explored using a scanning electron microscope (Apreo S LoVac, Czech) and a transmission electron microscope (JEOL JEM-F200, Japan), while the surface elements of all samples were analysed by elemental mapping (EDS). The hydrophilicity of the samples was detected by a contact Angle Measuring Instrument (SZ-CAMB3, Sunzern, China), while the specific surface area of all samples was quantified by the Brunauer-Emmett-Teller (BET) (Micromeritics ASAP 2460, America). Crystalline patterns of prepared samples were characterized by an X-ray diffractometer (XRD, Rigaku Ultima IV, Japan) with Cu Kα radiation at a scanning rate of $2°\cdot min^{-1}$. The content of the catalysts was analysed by thermogravimetry (TGA 550, America) from 25 to 800℃. Furthermore, the surface chemical states and surface defects of all samples were analysed by X-ray photoelectron spectroscopy (XPS, Thermo Scientific K-Alpha, America) and Raman spectroscopy (Horiba LabRAM HR Evolution, Japan) with 532 nm diode laser excitation. The properties of vacancies on the electrode surface were determined by electron paramagnetic resonance (EPR, Bruker EMXplus-6/1, Germany). The chemical bonds between elements were obtained by a Fourier Transform Infrared Spectrometer (FTIR, Thermo Fisher Scientific Nicolet iS20, America). The bandgap width of the semiconductor was obtained by Ultraviolet/Visible/Near-Infrared Diffuse Reflection Spectroscopy (UV-Vis DRS, Shimadzu UV-3600i Plus, Japan). The change of elements in solution was obtained from Ultraviolet-visible Spectrophotometer (UV-Vis, UV-2600i SHIMADZU, Japan). The thermal properties of the electrolyte were measured by a Differential Scanning Calorimeter (DSC, DSC25, TA, America).

Efficiency calculation

The efficiency (η_E) can be calculated by:[2]

$$\eta_E = \frac{V_{\text{cell}} \cdot \text{i}_{\text{cell}} - P_P}{\alpha_{\text{cell}} \cdot \text{i}_{\text{cell}} \cdot T_H + (1 - \varepsilon_{HX}) \cdot \rho \text{c}_\text{p} \cdot Q \cdot \Delta T - (\text{i}_{\text{cell}})^2 \cdot R_{in}}$$

Where V and i are the voltage and current of the battery respectively, P_p is the power consumption of the pump, α is the temperature coefficient of the full battery, ε_{HX} represents the heat exchange efficiency, ρ, c_P and Q represent the density, specific heat capacity and flow rate of the electrolyte respectively, and R_{in} is the internal resistance of the full battery. When Q is 74 μL/min, P_p can be simplified and ignored.

For TRFB with Co_3O_4@TGF/CoS_2@TGF at ΔT of 30K.

With heat recuperation (90%), the efficiency (η_E) was calculated:

$$\eta_E = \frac{31.6 \cdot 4.02 \cdot 10^{-6}}{2.0 \cdot 4.02 \cdot 10^{-6} \cdot 323 + (1 - 0.9) \cdot (1100 \cdot 3250 + 1100 \cdot 3320) \cdot \frac{74}{60} \cdot 10^{-9} \cdot 30 - \left(4.02 \cdot 10^{-3}\right)^2 \cdot 5}$$

=0.44%

The Carnot efficiency is η_c=9.28%

The relative Carnot efficiency is η_r=4.7%

Supplemental References

[1] A. D. Poletayev, I. S. McKay, W. C. Chueh, et al., Continuous electrochemical heat engines, Energy Environ. Sci., 2018, 11, 2964-2971.

[2] X. Qian, J. Shin, Y. Tu, et al., Thermally regenerative electrochemically cycled flow batteries with pH neutral electrolytes for harvesting low-grade heat, Phys. Chem. Chem. Phys., 2021, 23, 22501-22514.

[3] J. Bleeker, S. Reichert, J. Veerman, et al., Thermo-electrochemical redox flow cycle for continuous conversion of low-grade waste heat to power, Sci. Rep., 2022, 12, 7993.

[4] K. T. Xia, A. Rajan, Y. Surendranath, et al., Tunable electrochemical entropy through solvent ordering by a supramolecular Host, J. Am. Chem. Soc., 2023, 145, 25463-25470.

[5] Y. Yang, S. W. Lee, H. Ghasemi, et al., Charging-free electrochemical system for harvesting low-grade thermal energy, Proc. Natl. Acad. Sci. U. S. A., 2014, 111, 17011-17016.

[6] Y. Ding, X. Guo, K. Ramirez-Meyers, et al., Simultaneous energy harvesting and storage via solar-driven regenerative electrochemical cycles, Energy Environ. Sci., 2019, 12, 3370-3379.

[7] B. Yu, J. Duan, H. Cong, et al., Thermosensitive crystallization–boosted liquid thermocells for low-grade heat harvesting, Science, 2020, 370, 342-346.

[8] J. Duan, G. Feng, B. Yu, et al., Aqueous thermogalvanic cells with a high Seebeck coefficient for low-grade heat harvest, Nat. Commun., 2018, 9, 5146.

[9] S. M. Jung, S. Y. Kang, B. J. Lee, et al., Fe-N-C Electrocatalyst for Enhancing Fe

(II)/Fe (III) Redox Kinetics in Thermo-Electrochemical Cells, Adv. Funct. Mater., 2023, 33, 2304067.

[10] Z. Liu, D. Wu, S. Wei, et al., MXene hollow microsphere-boosted nanocomposite electrodes for thermocells with enhanced thermal energy harvesting capability, ACS Nano, 2025, 19, 3392-3402.

[11] A. Innocenti, S. Beringer and S. Passerini, Cost and performance analysis as a valuable tool for battery material research, Nat. Rev. Mater., 2024, 9, 347-357.

[12] H. Hu, M. Han, J. Liu, et al., Strategies for improving the design of porous fiber felt electrodes for all-vanadium redox flow batteries from macro and micro perspectives, Energy Environ. Sci., 2025, 18, 3085-3119.

[13] J. Huang, A. H. Clark, N. Hales, et al., Oxidation of interfacial cobalt controls the pH dependence of the oxygen evolution reaction, Nat. Chem., 2025, 17, 856-864.

[14] K. Zhang, C. Yan and A. Tang, Unveiling electrode compression impact on vanadium flow battery from polarization perspective via a symmetric cell configuration, J. Power Sources, 2020, 479, 228816.

[15] K. Zhang, J. Xiong, C. Yan, et al., In-situ measurement of electrode kinetics in porous electrode for vanadium flow batteries using symmetrical cell design, Appl. Energy, 2020, 272, 115093.

[16] P. Liu, B. Yu, Y. Zeng, et al., Thermosensitive slurry electrolyte design for efficient electrochemical heat harvesting, Energy Environ. Sci., 2025, 18, 2852-2860.